Supplementary Materials for

"Ultra-Clean Angstroporous Monolayer Amorphous Carbon Yields High Precision Proton Beam"

Huihui Lin[1, 8], Jian Jiang[2, 3, 8], Yanxin Dou[4, 8], Pin Lyu[1, 8], Xiaocang Han[5], Yuan Meng[5], Yuanyuan He[1], Xin Zhou[1,7], KangShu Li[5], Guoming Lin[1], Yu Teng[1], Jinxing Chen[1], Yang Meng[1], Thomas Osipowicz[4], Xiaoxu Zhao[5], Xiao Cheng Zeng[2, 6*] and Jiong Lu[1, 7*]*

[1] Department of Chemistry, National University of Singapore, Singapore 117543, Singapore

[2] Department of Materials Science and Engineering, City University of Hong Kong, Hong Kong 999077, China

[3] Shenzhen Research Institute, City University of Hong Kong, Shenzhen 518057, China

[4] Centre for Ion Beam Applications, Department of Physics, National University of Singapore, Singapore 117542

[5] School of Materials Science and Engineering, Peking University, Beijing, China

[6] Hong Kong Institute of Clean Energy, City University of Hong Kong, Hong Kong 999077, China

[7] Institute for Functional Intelligent Materials, National University of Singapore, 117544, Singapore

[8]These authors contributed equally: Huihui Lin, Jian Jiang, Yanxin Dou, Pin Lyu

[*]e-mail: xiaoxuzhao@pku.edu.cn; xzeng26@cityu.edu.hk; chmluj@nus.edu.sg

Table of Contents

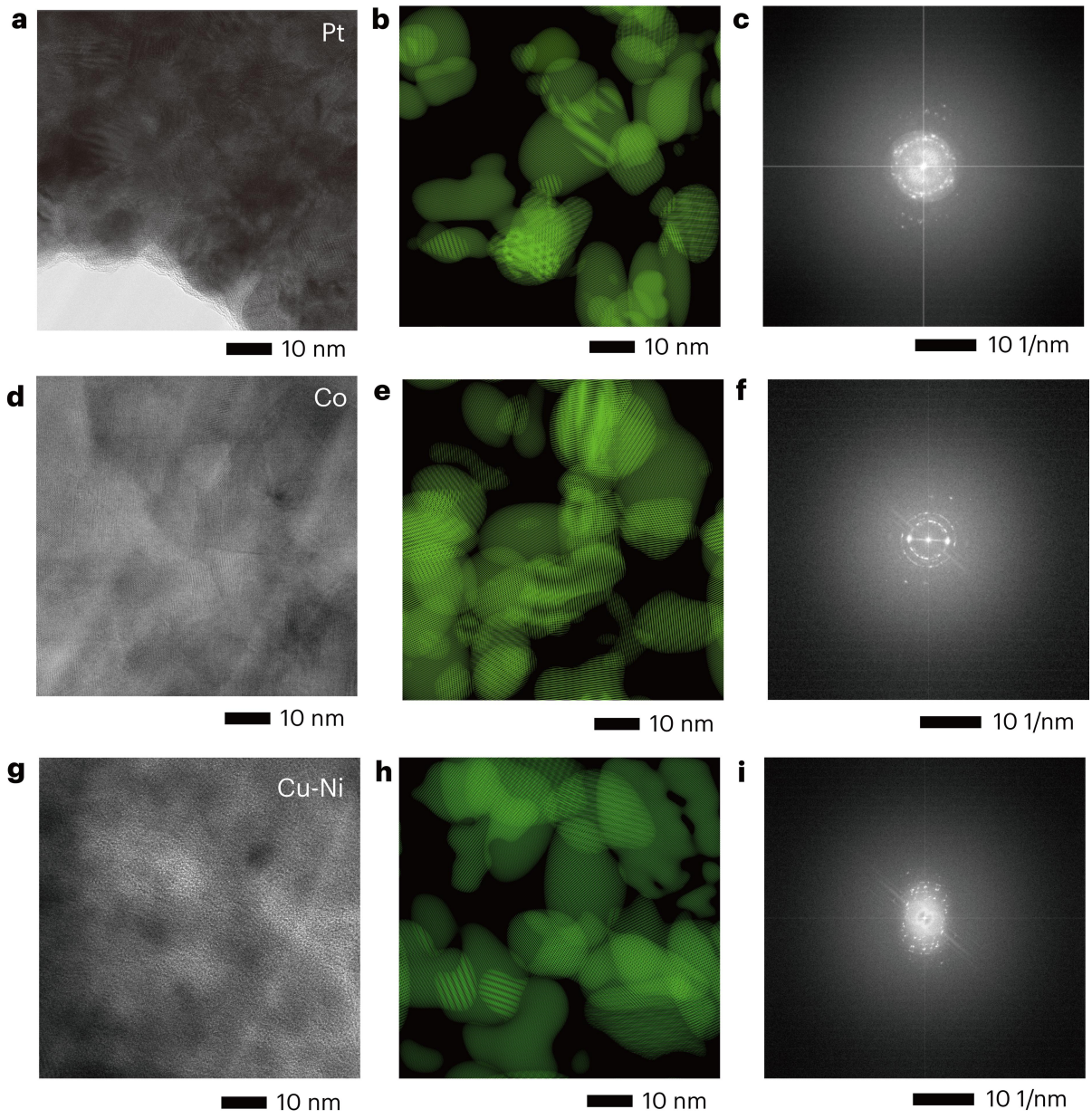

Supplementary Figure S1. Structural characterization of different Disorder-Subs. a, **d**, **g**, Low-magnification TEM images of different Disorder-Subs, including Pt, Co, and CuNi Disorder-Subs. **b**, **e**, **h**, Corresponding false-colored TEM images highlighting grain structures. **c**, **f**, **i**, Corresponding SAED patterns, revealing irregular grains with sizes of several tens of nanometers.

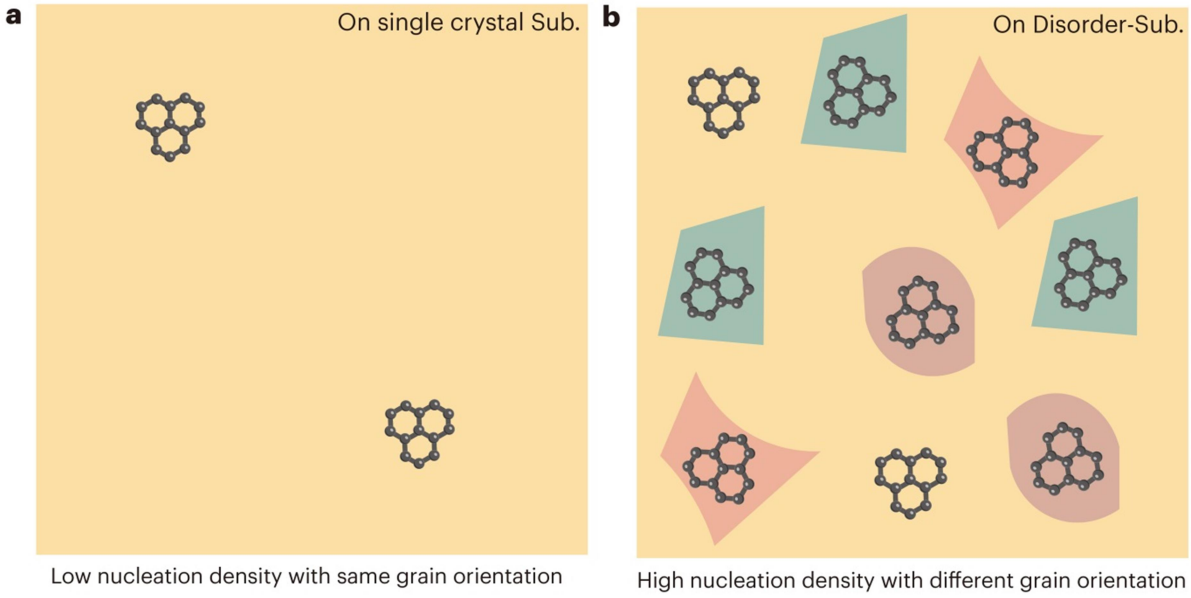

Supplementary Figure S2. The schematic illustration of the nucleation mechanism on single crystal substrate and Disorder-Sub. **a**, Low nucleation density with same grain orientation for SCG on single crystal substrate. **b**, High nucleation density with different grain orientation for MAC on Disorder-Sub, where the Macaron blue, pink, and purple regions represent nanograins within the Disorder-Sub, each exhibiting different grain orientations.

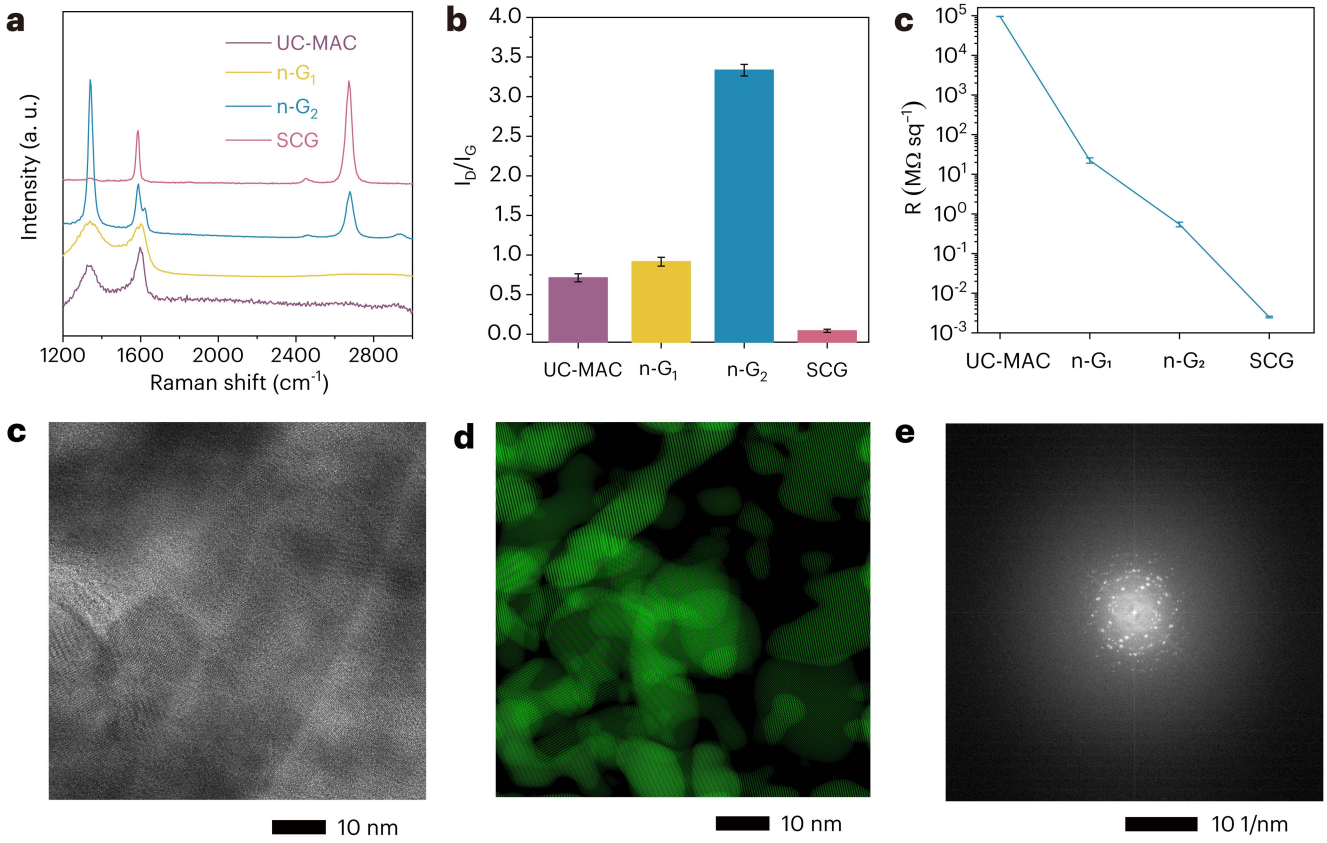

Supplementary Figure S3. Raman spectrum and sheet resistance of as-grown monolayer carbon films by DTD growth. (a) Raman spectrum, (b) Ratio of Raman intensity of D peak to G peak (I_D/I_G) and (c) Sheet resistance of the as-grown monolayer carbon. The Ratio of Raman intensity in (b) is extracted from (a). The most prominent features in the Raman spectra of monolayer carbon are the D band, G band, and 2D band[1,2]. The G band is associated with the doubly degenerate (iTO and LO) phonon mode, where the two sublattices vibrate relative to each other (q = 0). The D band corresponds to the iTO phonon and is linked to non-hexagonal ring structures. The 2D band originates from a second-order process, involving two iTO phonons near the K point. Therefore, UC-MAC exhibits higher noise compared to the other three films[3,4]. **d-e,** Structural characterization of Cu Disorder-Subs. (d) Low-magnification TEM images of different Disorder-Subs, including Cu Disorder-Subs. (e) Corresponding false-colored TEM images highlighting grain structures. (f) Corresponding SAED patterns, revealing irregular grains with sizes of several tens of nanometers. We used false-colored TEM images derived from SAED patterns to examine the atomic structures of the Cu Disorder-Subs, which revealed irregular grains with varied crystallographic orientations and sizes on the order of several tens of nanometers (d-f). While overlapping regions may occur due to the spatial resolution limits of SAED, these results confirm the disordered nature of the Cu substrate. The AFM phase images complement this view by providing surface morphology at the nanoscale, although minor discrepancies in texture appearance are expected due to different imaging modalities.

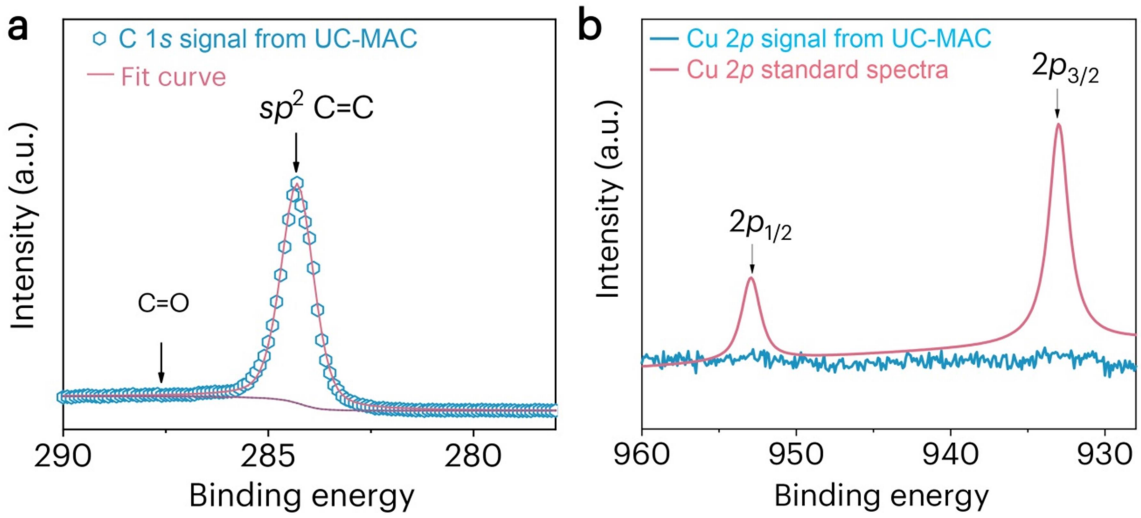

Supplementary Figure S4. (**a**) C 1*s* XPS spectra and (**b**) Cu 2*p* XPS spectra of as-grown UC-MAC on SiO_2 substrates. No detectable Cu 2*p* signal is observed from UC-MAC in (**b**), using Cu 2*p* standard spectra as reference.

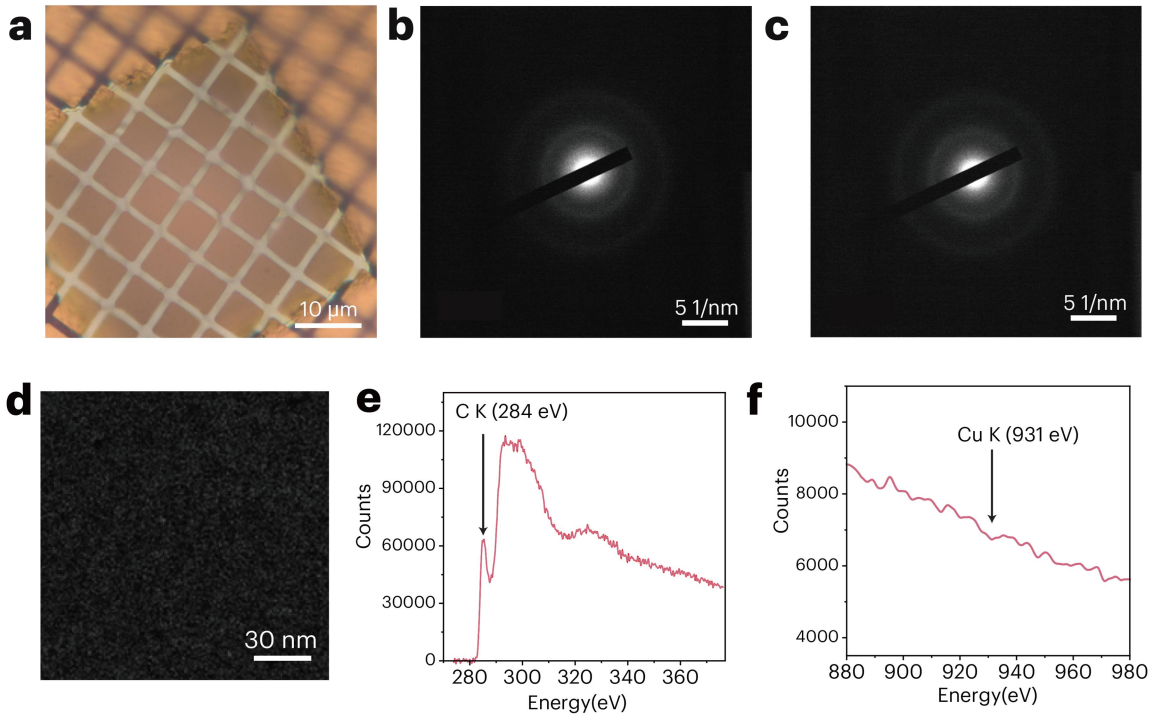

Supplementary Figure S5. STEM/SAED/EELS characterization of UC-MAC. a, Optical microscopic image of the as-grown UC-MAC film. **b-c**, Corresponding SAED patterns acquired from (**a**) at two randomly selected sites over a ~210 nm × 210 nm selected area aperture. (**d–f**) Core-loss EELS spectrum from (d), showing a distinct C K edge peak (e), with no detectable Cu peak (**f**) acquired at the same site, confirming the absence of Cu in the UC-MAC film.

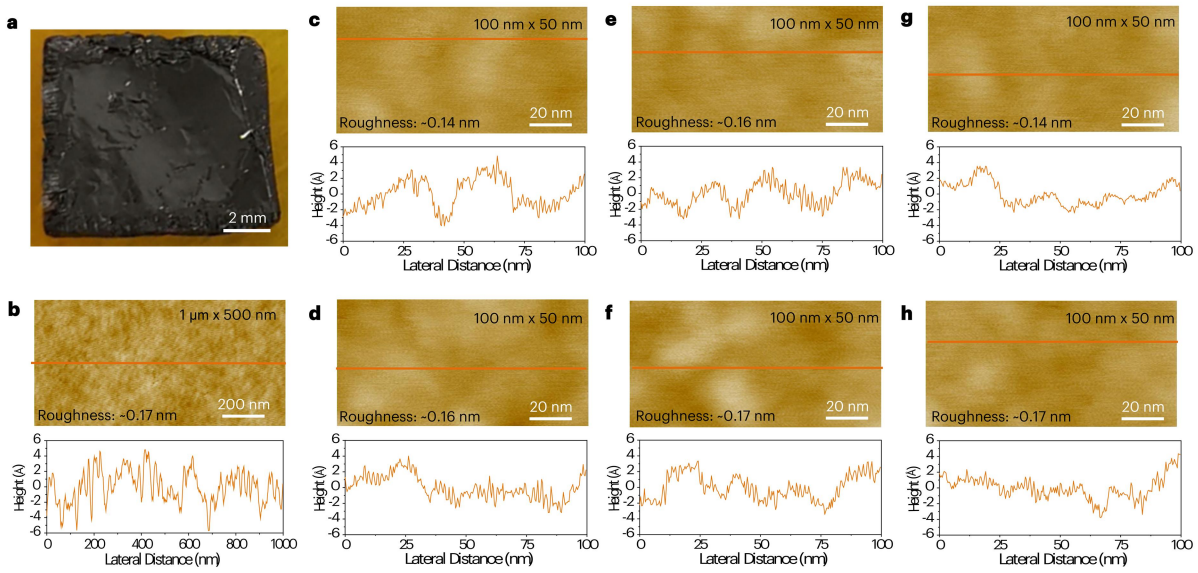

Supplementary Figure S6. a, **b**, Optical microscopic image (**a**) and AFM image of a 1 μm × 500 nm area (**b**) of as-grown UC-MAC transferred onto an HOPG substrate, demonstrating an ultra-clean surface. **c**-**h**, Smoothness of the as-grown films on HOPG substrate by AFM acquired at six randomly selected regions (100 nm × 50 nm), revealing an average smoothness of ~ 0.16 nm.

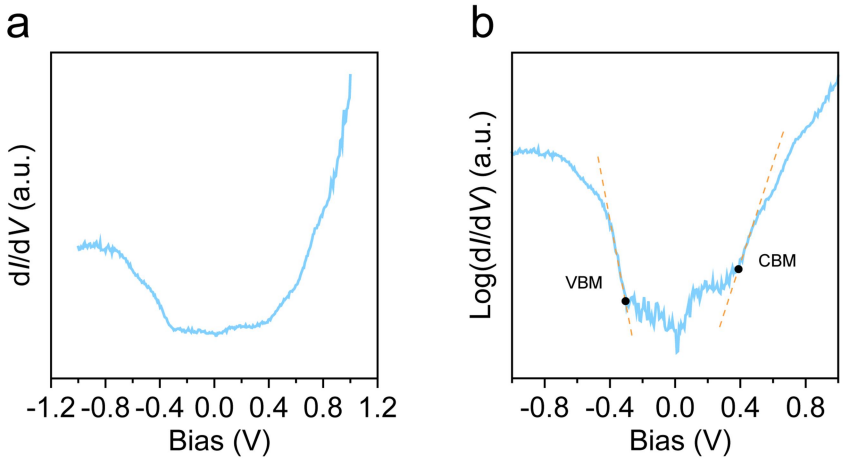

Supplementary Figure S7. a, Band edge determination through the analysis of the dI/dV spectrum taken over UC-MAC on HOPG. **b**, logarithmic scaled dI/dV spectrum of a to better determine the band edges.

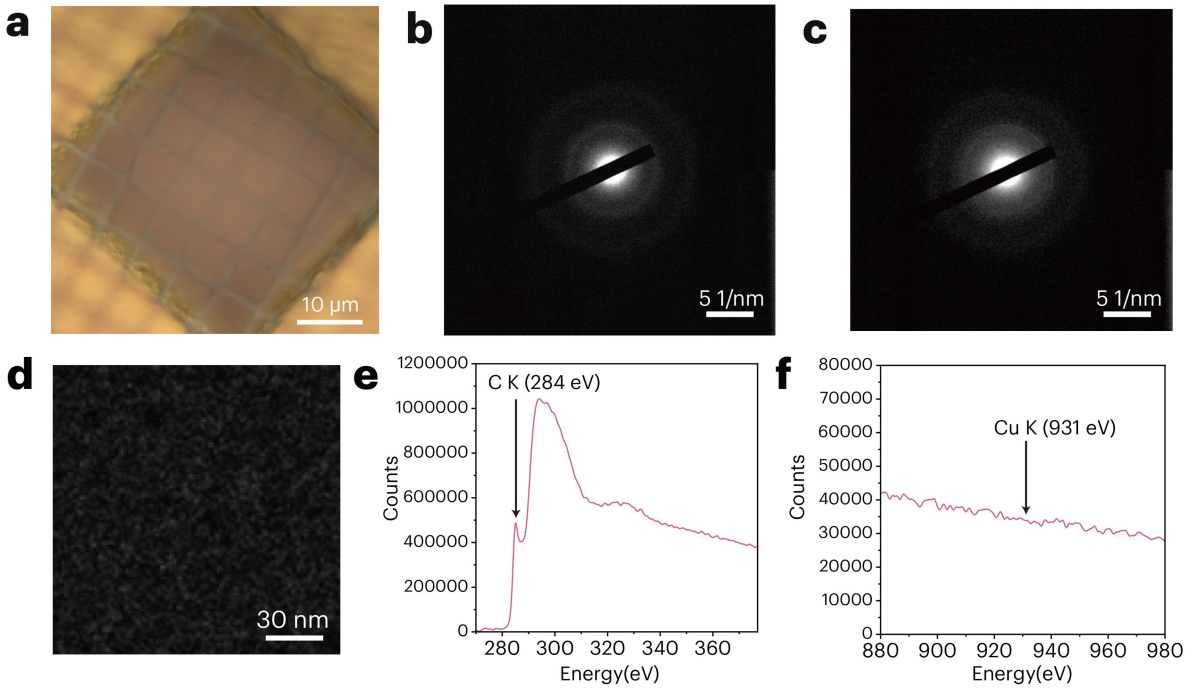

Supplementary Figure S8. STEM/SAED/EELS characterization of n-G_1. a, Optical microscopic image of the as-grown n-G_1. **b-c**, Corresponding SAED patterns acquired from (**a**) at two randomly selected sites over a ~210 nm × 210 nm selected area aperture. (**d–f**) Core-loss EELS spectrum from (d), showing a distinct C K edge peak (e), with no detectable Cu peak (**f**) acquired at the same site, confirming the absence of Cu in the n-G_1 film.

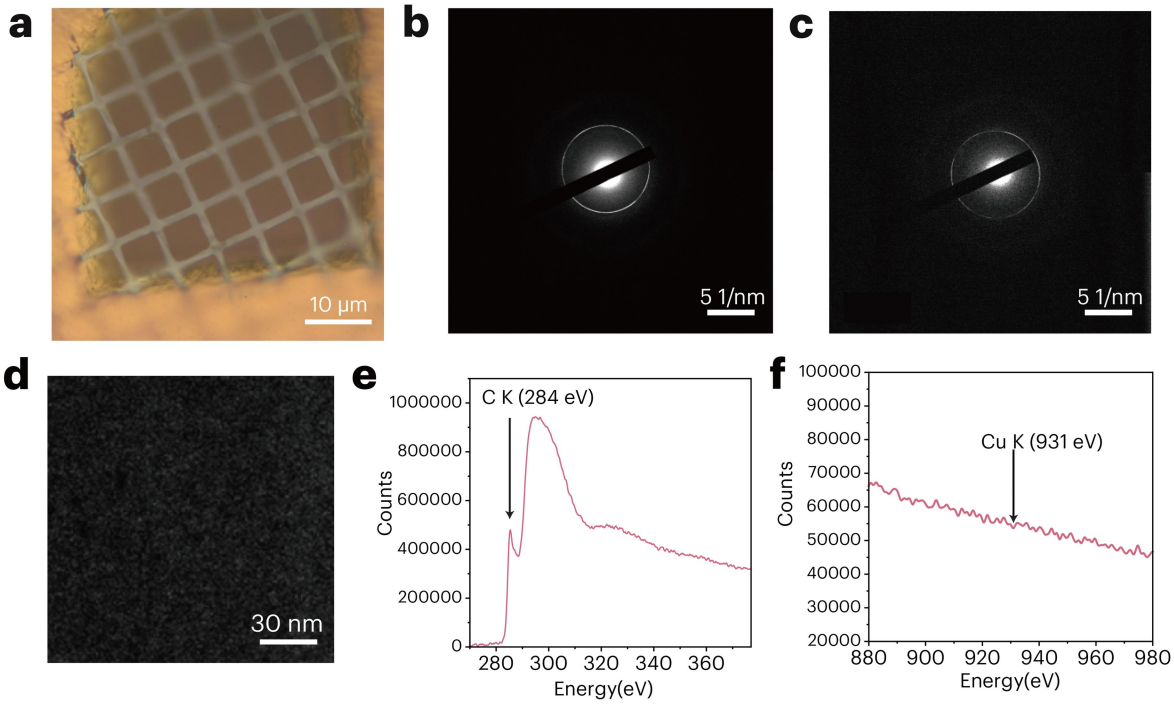

Supplementary Figure S9. STEM/SAED/EELS characterization of n-G_2. a, Optical microscopic image of the as-grown n-G_2. **b-c**, Corresponding SAED patterns acquired from (**a**) at two randomly selected sites over a ~210 nm × 210 nm selected area aperture. (**d–f**) Core-loss EELS spectrum from (d), showing a distinct C K edge peak (e), with no detectable Cu peak (**f**) acquired at the same site, confirming the absence of Cu in the n-G_2 film.

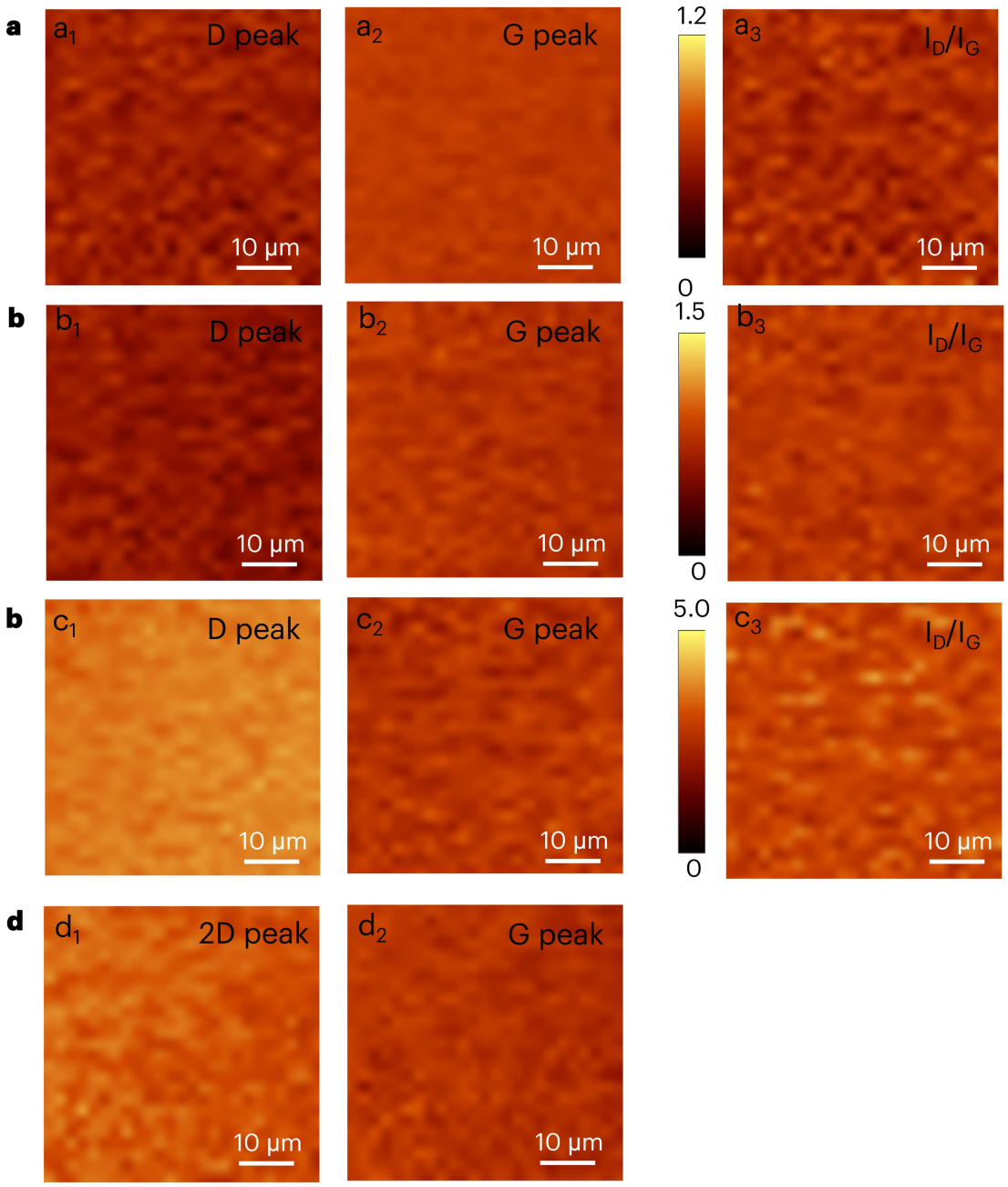

Supplementary Figure S10. Raman mapping of the as-grown films on SiO_2/Si substrates (50 ×50 μm^2 , with 2,500 data points). **a**, UC-MAC: **a$_1$**, D peak; **a$_2$**, G peak; **a$_3$**, I_D/I_G ratio. **b**, n-G_1: **b$_1$**, D peak; **b$_2$**, G peak; **b$_3$**, I_D/I_G ratio. **c**, n-G_2: **c$_1$**, D peak; **c$_2$**, G peak; **c$_3$**, I_D/I_G ratio. **d**, SCG: **d$_1$**, 2D peak; **d$_2$**, G peak. For SCG, the D peak is negligible, so the I_D/I_G ratio is not included.

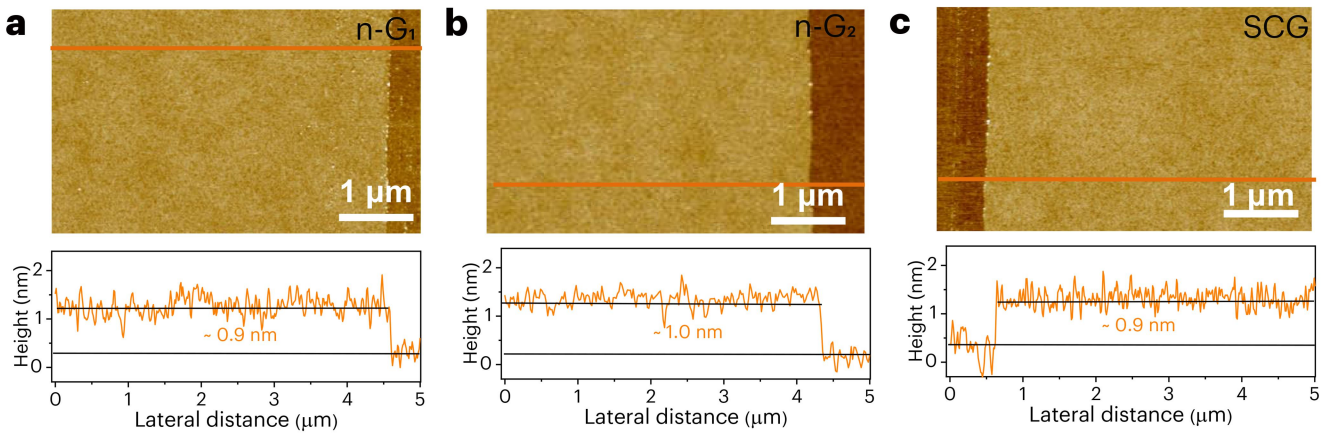

Supplementary Figure S11. AFM images and the corresponding height profiles of (**a**) n-G_1, (**b**) n-G_2, (**c**) SCG on SiO_2/Si substrates.

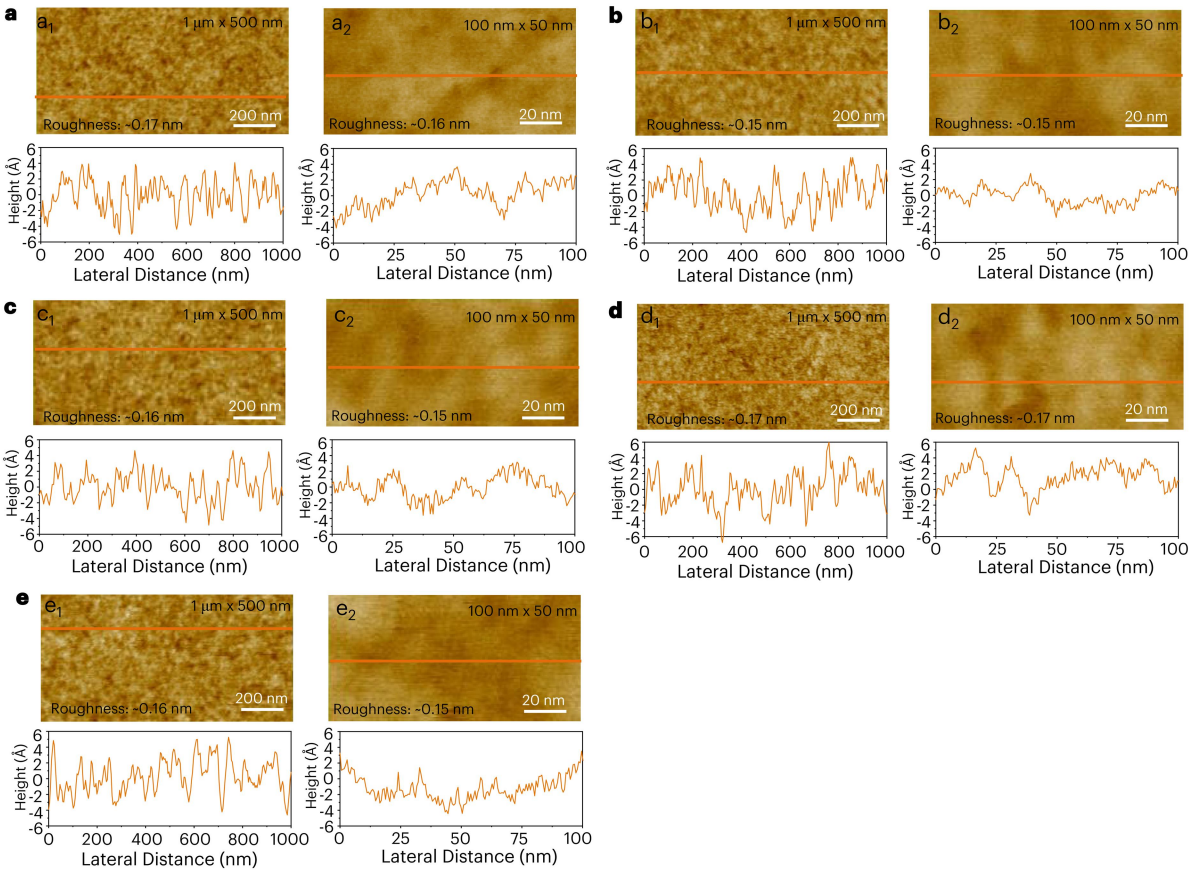

Supplementary Figure S12. Smoothness of the as-grown films by AFM on SiO_2/Si substrates. **a**, UC-MAC. **b**, n-G_1**; c**, n-G_1; **d**, SCG. The as-grown films exhibit similar smoothness to the SiO_2/Si substrate (**e**).

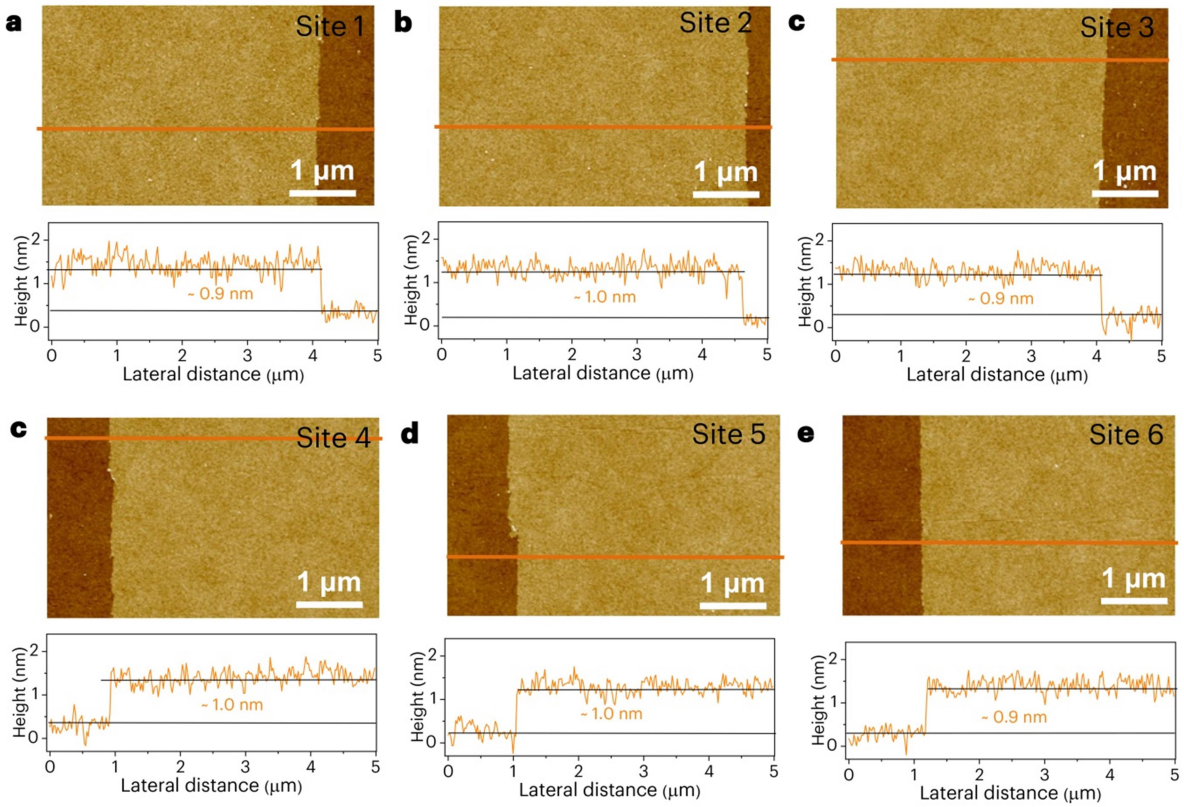

Supplementary Figure S13. AFM images and the corresponding height profiles of the as-grown 8 inch UC-MAC on SiO_2/Si substrate taken at six randomly selected regions.

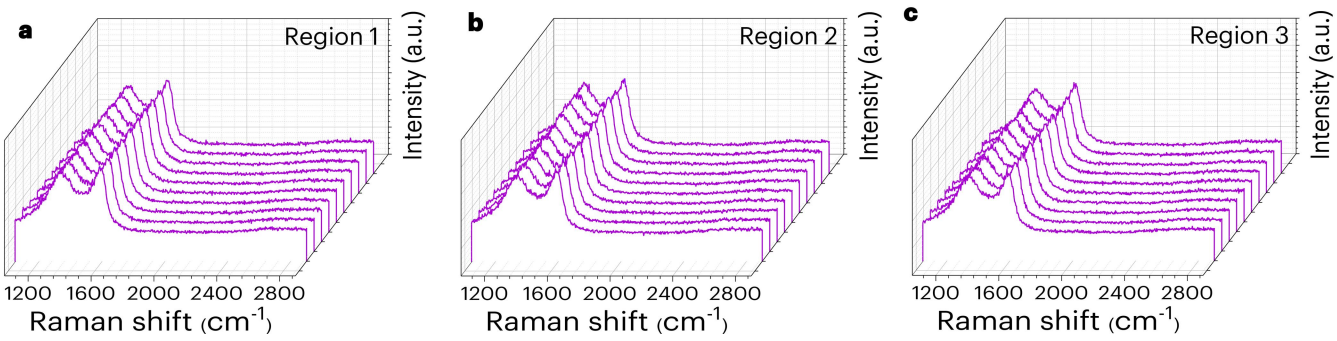

Supplementary Figure S14. Raman spectrum of as-grown 8 inch UC-MAC on SiO_2/Si substrate taken at 30 randomly selected sites.

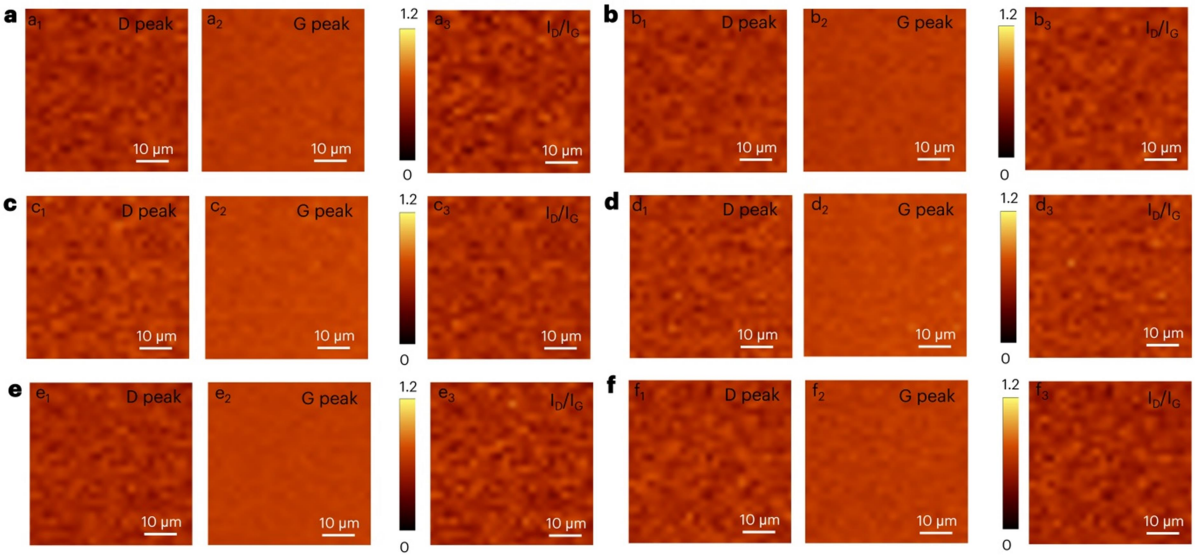

Supplementary Figure S15. Raman mapping of the as-grown 8 inch UC-MAC on SiO_2/Si substrates (50 ×50 μm^2 , with 2,500 data points) taken at six randomly selected regions.

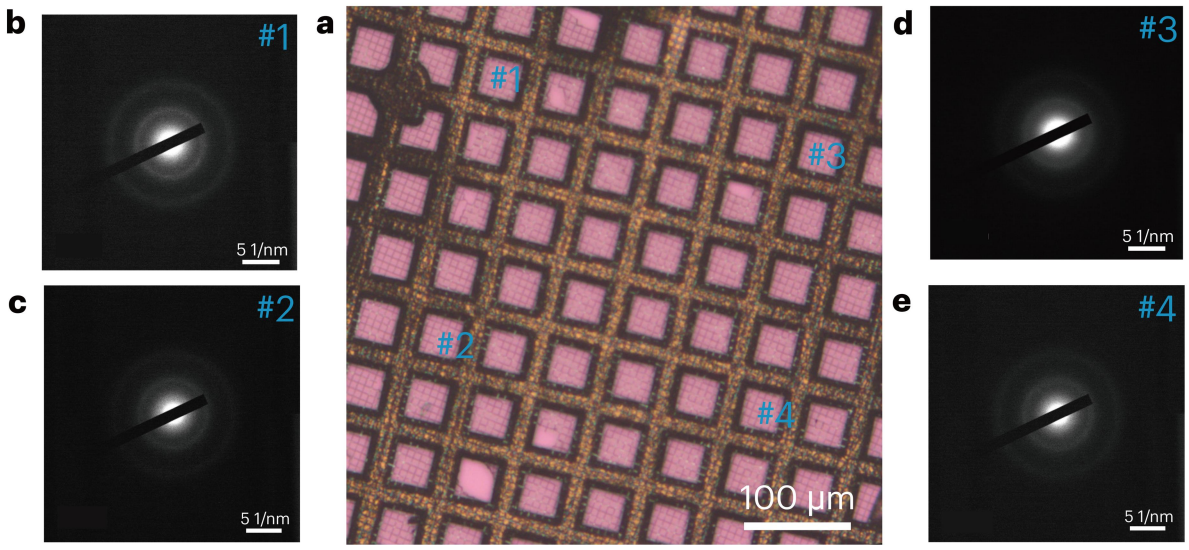

Supplementary Figure S16. STEM/SAED characterization from 8 inch UC-MAC. a, Optical microscopic image of the as-grown UC-MAC film. **b-e**, Corresponding SAED patterns acquired from (**a**) at four randomly selected sites over a ~210 nm × 210 nm nm selected area aperture.

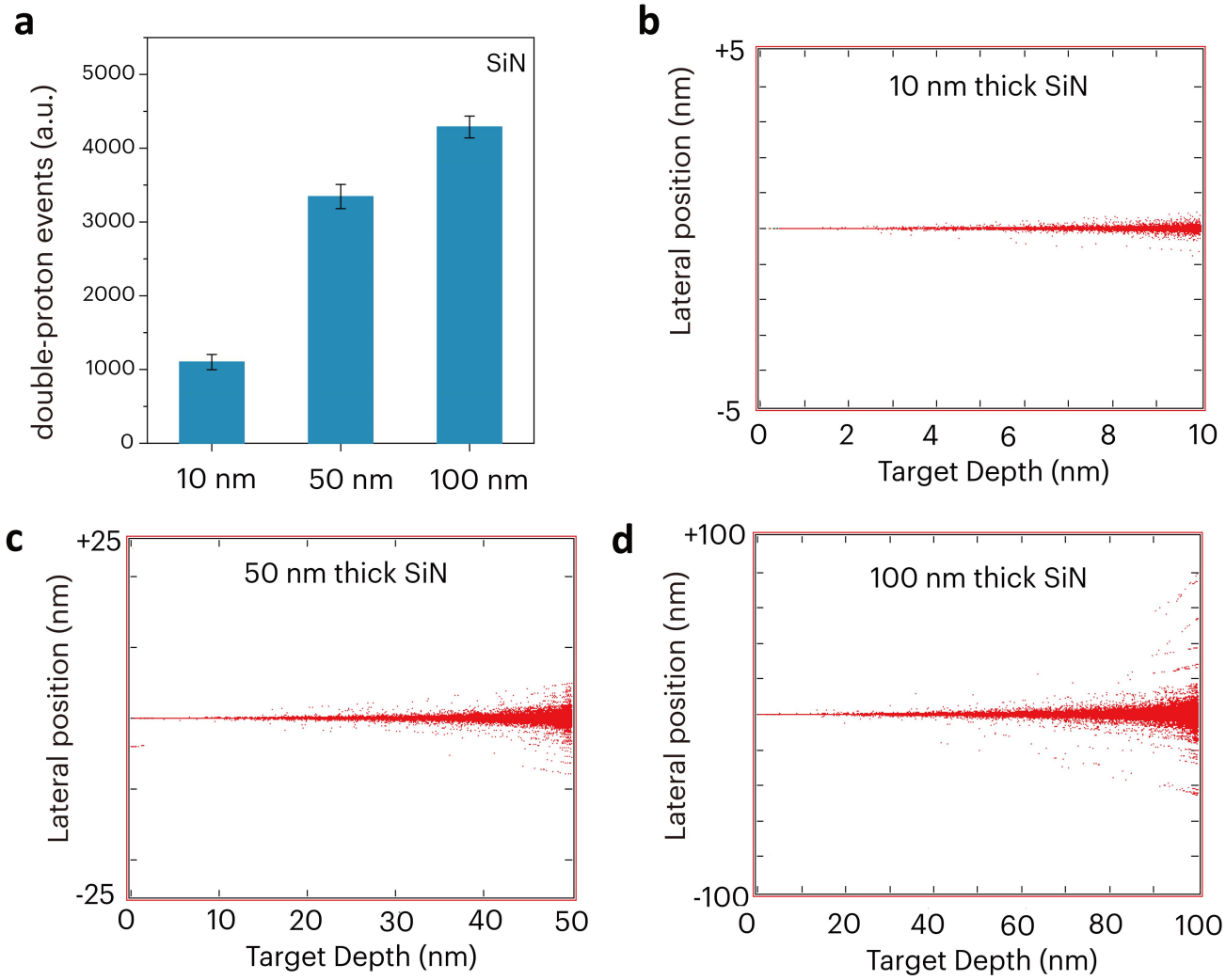

Supplementary Figure S17. Splitting of single hydrogen molecular ions on ultrathin SiN films. a, Thickness of SiN dependent double-proton events of hydrogen molecular ions. **b-d**, The Stopping and Range of Ions in Matter (SRIM) simulations of 0.75 MeV proton trajectories in SiN film of varying thickness: (b) 10 nm thick, (c) 50 nm thick, (d) 100 nm thick. The fragment protons from 1.5 MeV hydrogen molecular ions have an energy of 0.75 MeV.

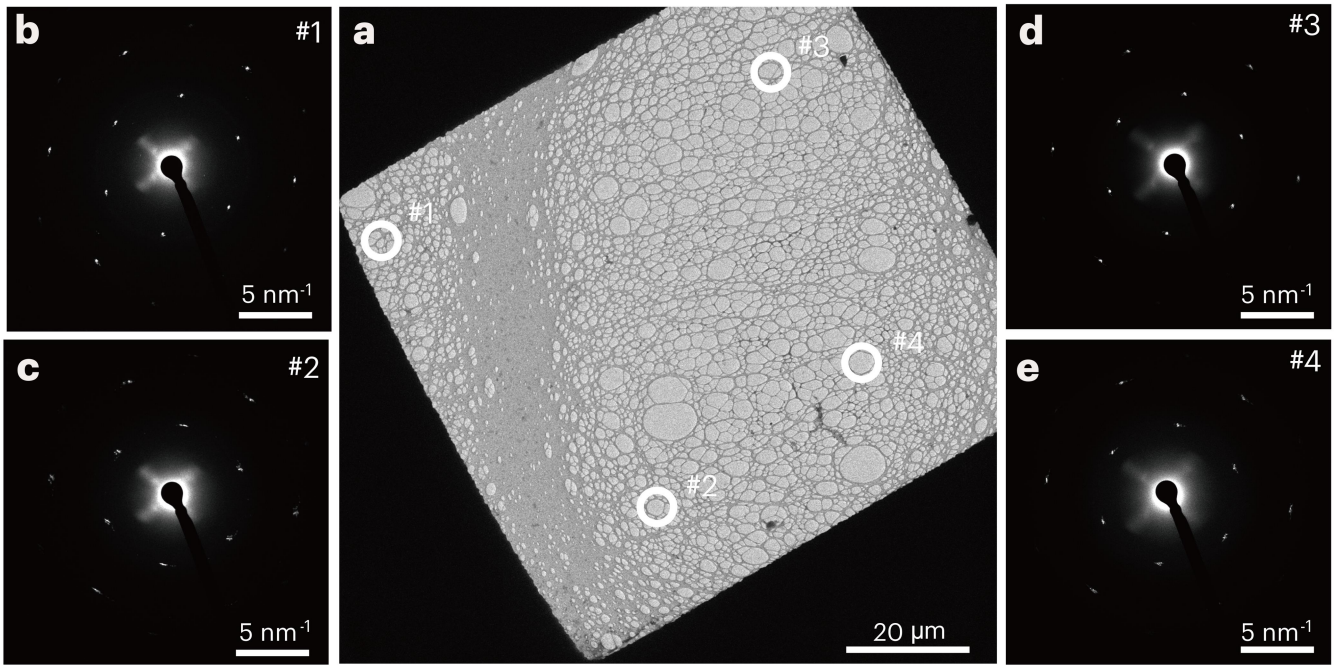

Supplementary Figure S18. TEM image of SCG grown from as-sputtered single crystal Cu(111) substrate. a-e, Low magnification TEM image of SCG (a) and the SAED (b-e) of the marked sites in (a) proved that the SCG has the same crystal orientation.

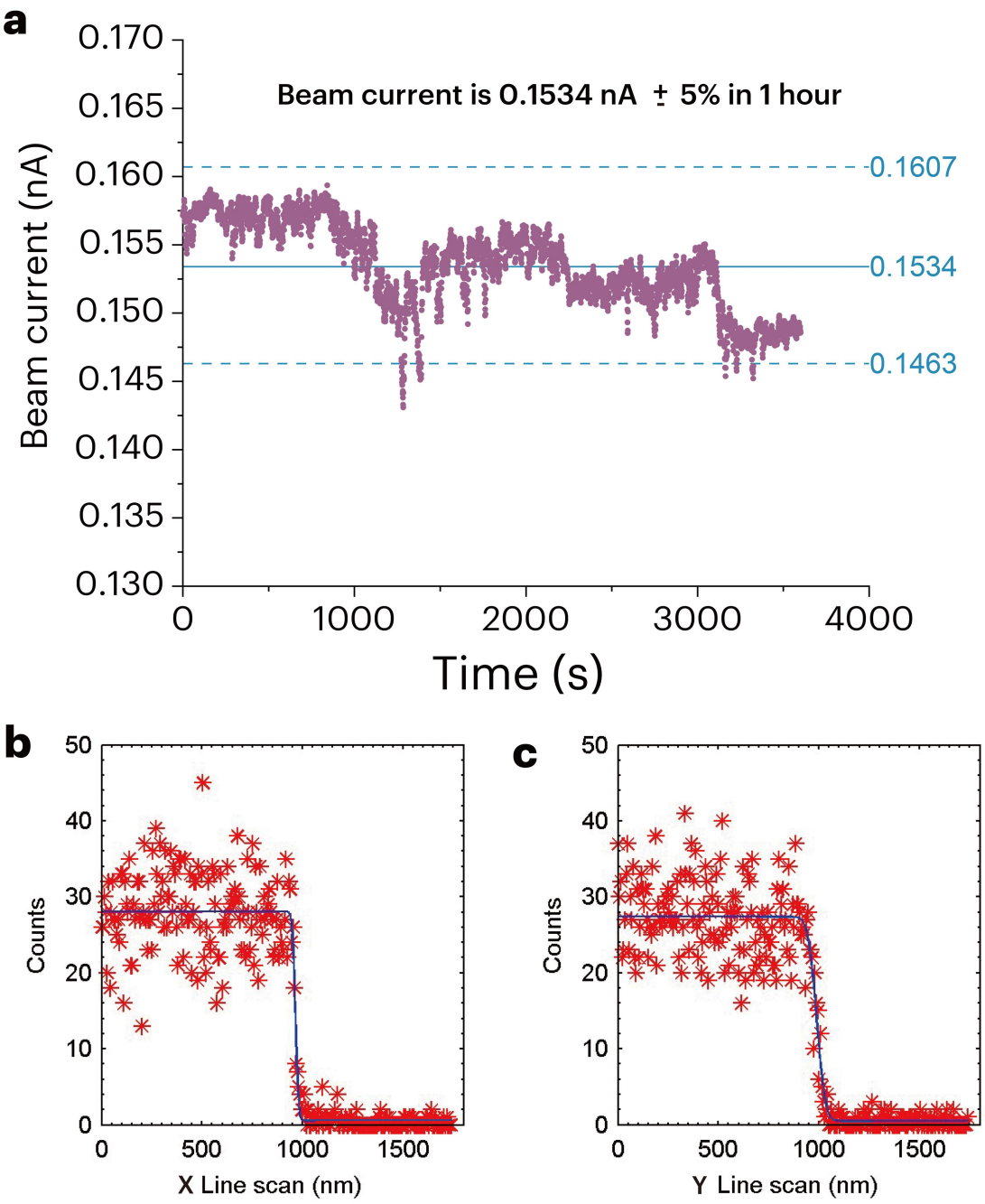

Supplementary Figure S19. Performance of the high energy ion nanobeam for splitting of hydrogen molecular ions. a, Typical long-term beam current stabilities data. **b, c**, Focused beam spot size (FWHM) of 28 nm×80 nm.

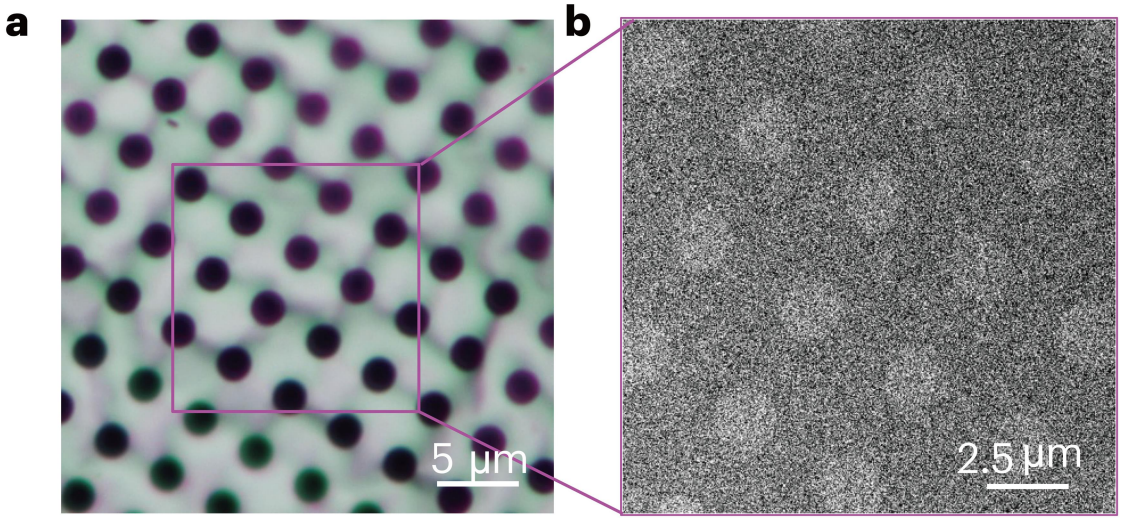

Supplementary Figure S20. Suspended SCG on Au grid. a, Optical microscopic image of suspended ultra-clean SCG on Au grid. **b,** Near-axis STIM image of the area marked out by a purple square in (**a**).

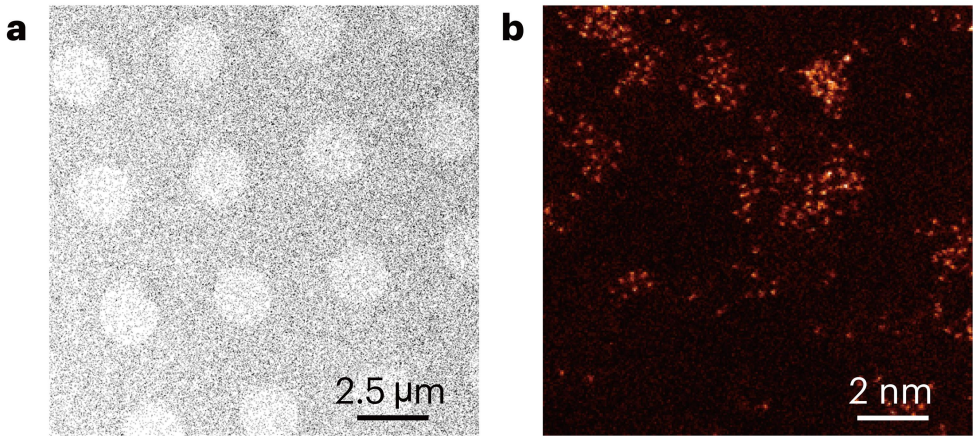

Supplementary Figure S21. Non-clean MAC with the surface decorated with metal impurities. a-b, near-axis STIM image (**a**) and atomically resolved ADF-STEM image (**b**) of non-clean MAC grown at a low temperature of 460 °C, revealing the surface decoration with metal atom/clusters.

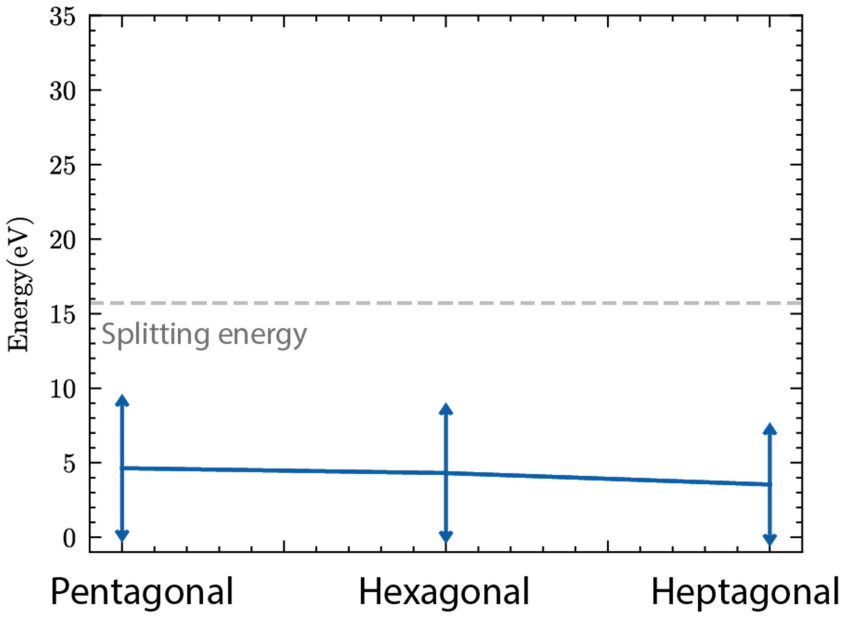

Supplementary Figure S22. Computed energy barrier for the first-step splitting of H_2^+ when the frontend H_A atom passes through either the hexagonal or non-hexagonal (pentagonal or heptagonal) ring. The initial H_2^+ ion being in the vertical configuration toward SCG/UC-MAC monolayer.

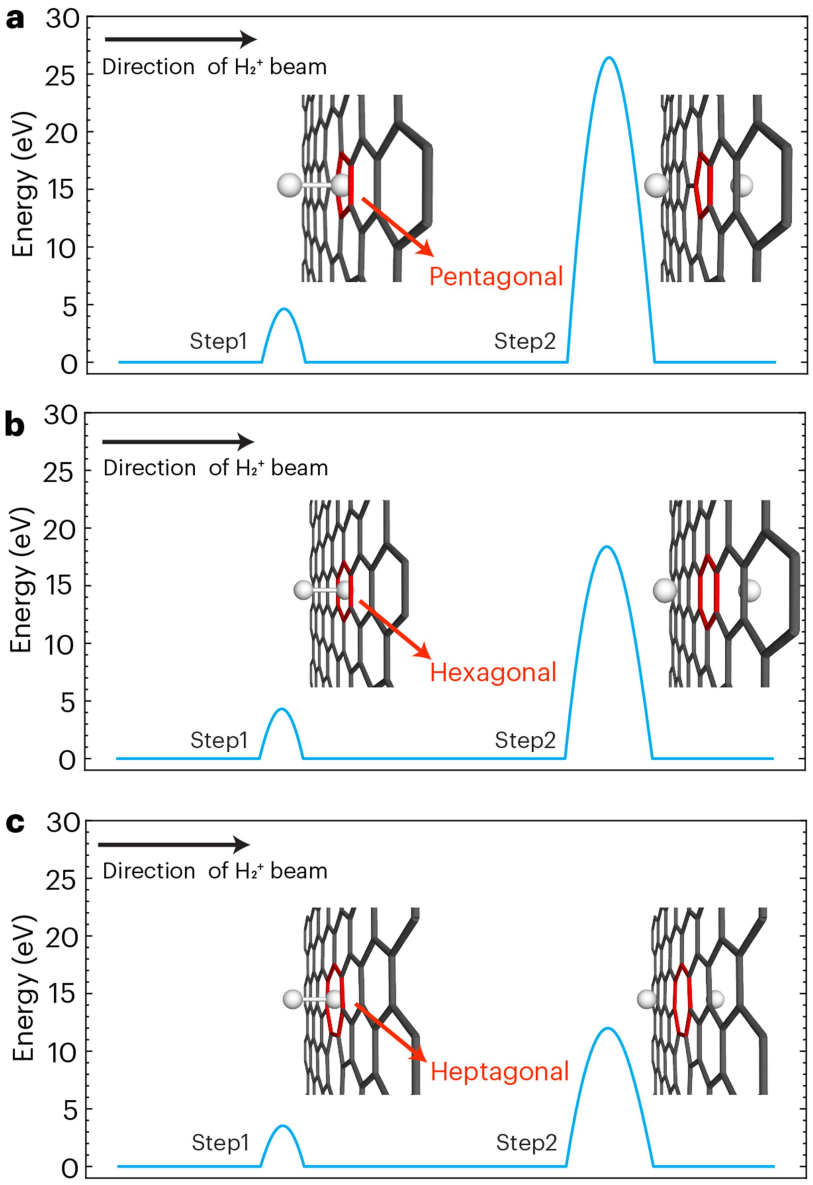

Supplementary Figure S23. Schematic energy profile of an H_2^+ (in a vertical configuration) passing through a MAC with (**a**) pentagonal, (**b**) hexagonal, and (**c**) heptagonal carbon rings. The white spheres represent the H atoms, while the penetrated polygonal carbon structure is in red.

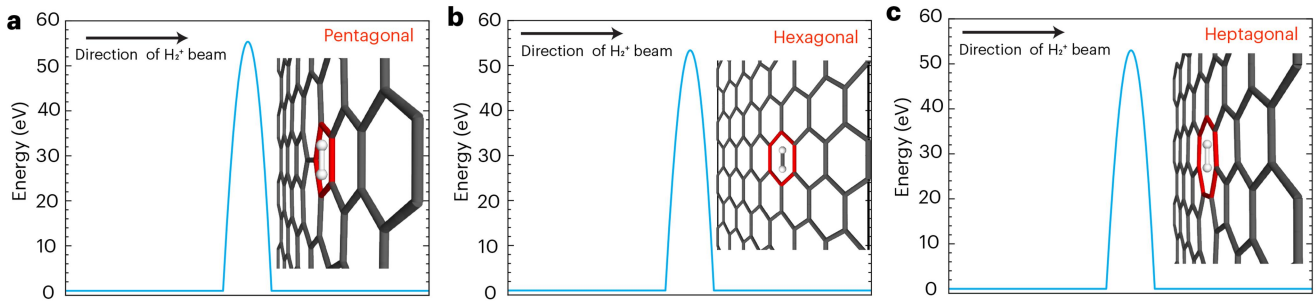

Supplementary Figure S24. Schematic energy profile of an H_2^+ (in a parallel configuration) passing through a MAC with (**a**) pentagonal, (**b**) hexagonal, and (**c**) heptagonal carbon structures. The white spheres represent the H atoms, while the penetrated polygonal carbon structure is red.

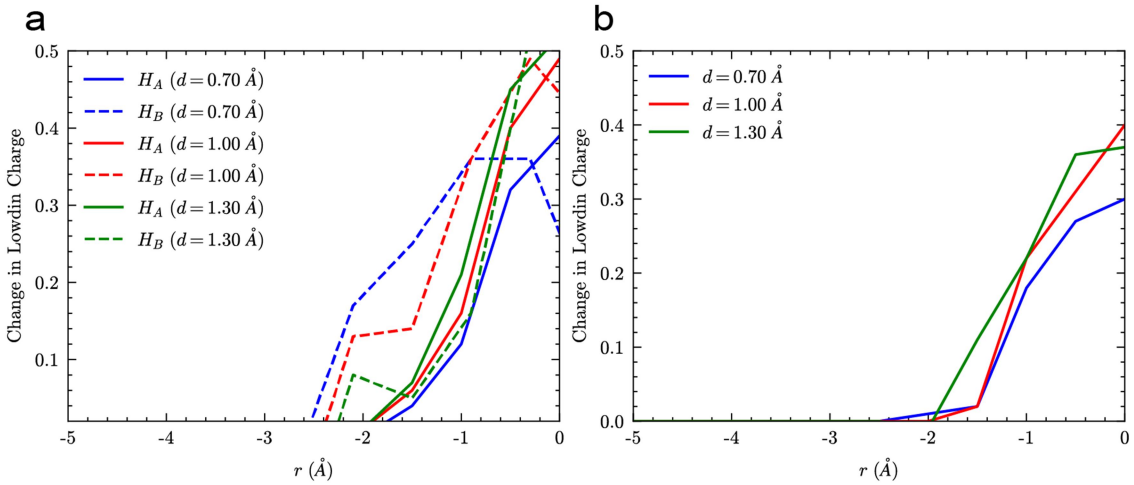

Supplementary Figure S25. Charge analysis of individual H in the H_2^+ ion when approaching to the graphene monolayer at different H-H bond distance (*d*), and in different initial H_2^+ configuration: (a) Vertical and (b) parallel. Here, *r* refers to the distance between the hydrogen atom and the graphene layer in (a), or between the center of mass of H_2^+ ion and the graphene layer in (b). The position of the graphene layer is at 0.

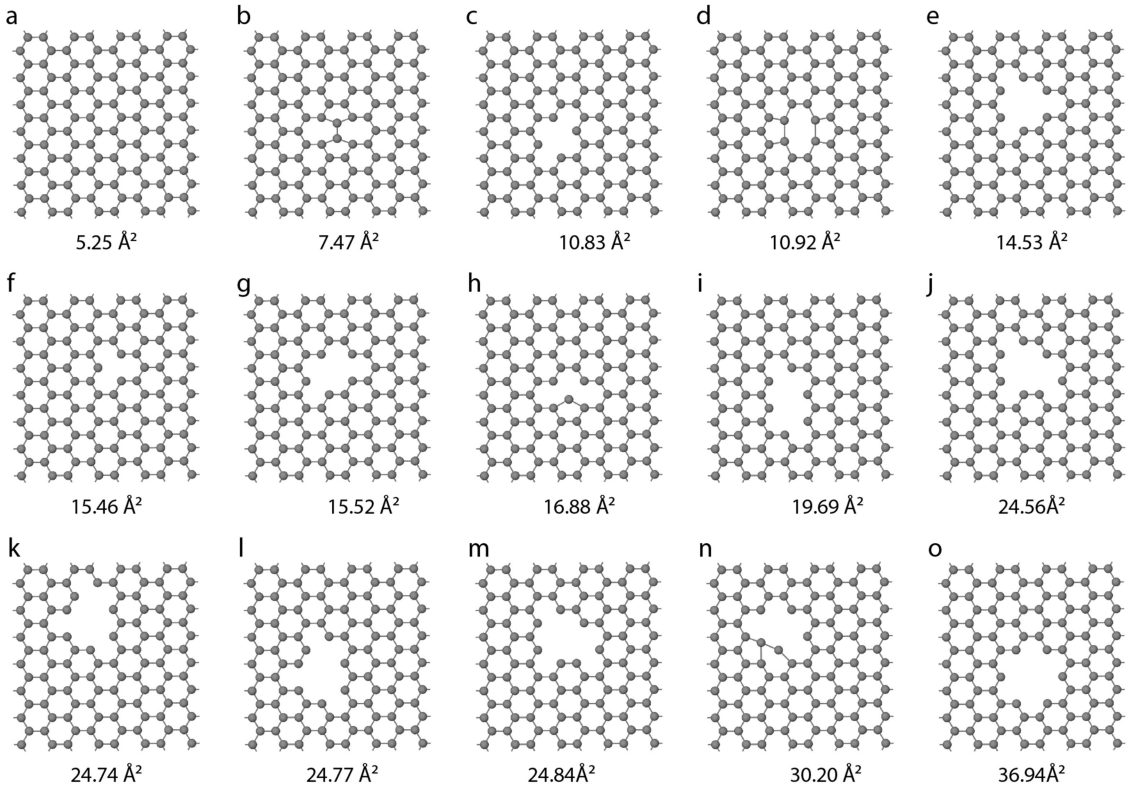

Supplementary Figure S26. Computed geometric area of various defect or pores (b-o) carved in atomic structure model of graphene.

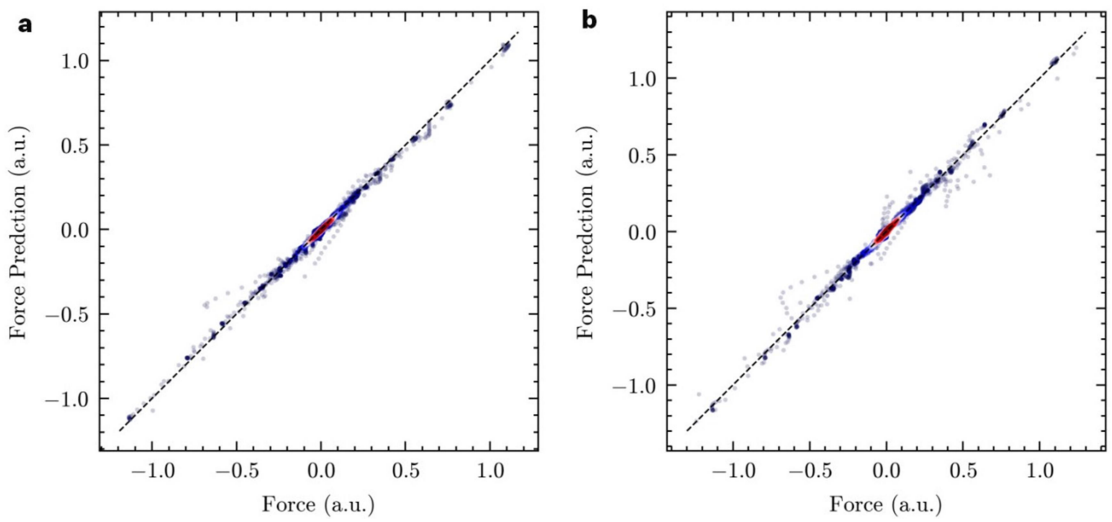

Supplementary Figure S27. The training results of MLP based on the (**a**) linear and (**b**) binary step model of electron transfer.

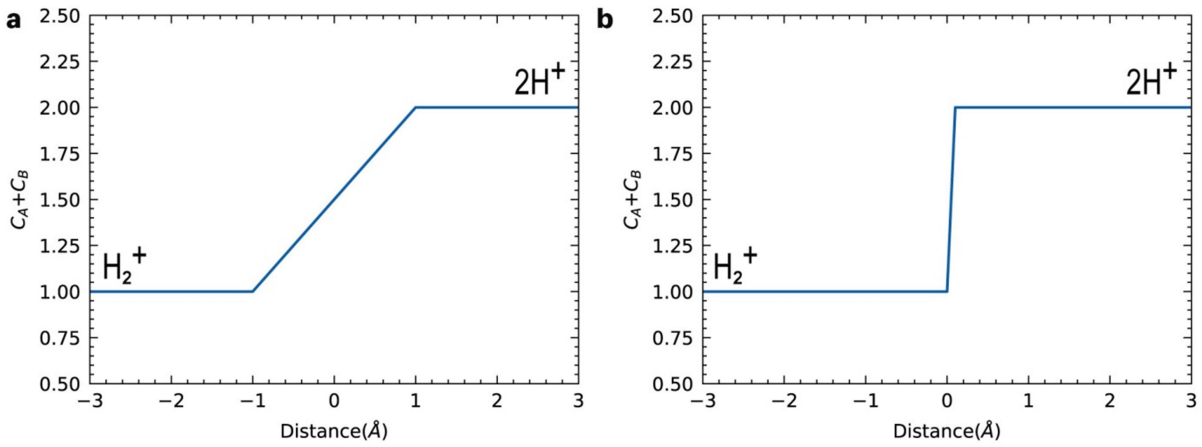

Supplementary Figure S28. The charge transfer scheme based on the (**a**) linear and (**b**) binary step model.

Table 1. **Sputtering parameters for different sputtered substrates.**

Sputtered substrate	Thickness (nm)	Metal deposition rate (Å/s)	Substrate temperature (°C)	Nanograins density
Cu (111)	1000	0.5	800	0
Cu Disorder-Sub	50	0.1	200	~2260±20 /um^2
Cu substrate #1	50	0.1	200	~2260±20 /um^2
Cu substrate #2	150	0.5	500	~72±12 /um^2

Note: Cu substrate #1 and Cu Disorder-Sub were sputtered under the same conditions.

Table 2. Representative CVD preparation methods of monolayer graphene/amorphous carbon.

Monolayer carbon film	Preparation method	Carbon source	Growth temperature/ °C	Growth time/s	Refs.
Graphene	CVD	CH_4	1000	1800	*Science, 2009, 324, 1312-1314.*[5]
Graphene	CVD	C_2H_4	~727	3600	*Nature, 2021, 596, 519-524.*[6]
Graphene	ICP-CVD	CH_4	750	300	*Nature, 2014, 505, 190-194.*[7]
n-G	ICP-CVD	CH_4	750 ~ 800	150	*2D Materials, 2016, 3, 021001.*[8]
MAC	Laser-assisted depositions	CH_4	200 ~ 500	60 ~ 600	*Nature, 2020, 577,199-203.*[3]
MAC	CVD	BN-doped $C_{10}H_6Br_2$	300 ~ 500	300 ~ 1800	*Nature, 2023, 615, 56-61.*[4]
UC-MAC	**Disorder-to-disorder synthesis**	**CH_4**	**820**	**3 ~ 20**	**This work**

Table 3. Specific DTD growth parameters of the as-grown monolayer carbon films in our work.

Sample	Sputtered substrate	Power/W	Growth temperature/ °C	Growth time/s
SCG	Cu (111)	50	820	300
n-G_1	Cu Disorder-Sub	20	820	60
n-G_2	Cu Disorder-Sub	20	820	30
UC-MAC	Cu Disorder-Sub	100	820	3~20
n-G_3	Cu substrate #1	50	820	30
n-G_4	Cu substrate #2	50	820	30

Adjusting the reaction power and growth duration allows fine-tuning of the density of non-hexagonal rings in the film. With these optimized parameters, various monolayer carbon films can be produced, ranging from SCG to UC-MAC.

References

1 Wu, J.-B., Lin, M.-L., Cong, X., Liu, H.-N. & Tan, P.-H. Raman spectroscopy of graphene-based materials and its applications in related devices. *Chem. Soc. Rev.* **47**, 1822-1873 (2018).

2 Malard, L. M., Pimenta, M. A., Dresselhaus, G. & Dresselhaus, M. S. Raman spectroscopy in graphene. *Physics reports* **473**, 51-87 (2009).

3 Toh, C.-T. *et al.* Synthesis and properties of free-standing monolayer amorphous carbon. *Nature* **577**, 199-203 (2020).

4 Tian, H. *et al.* Disorder-tuned conductivity in amorphous monolayer carbon. *Nature* **615**, 56-61 (2023).

5 Li, X. *et al.* Large-area synthesis of high-quality and uniform graphene films on copper foils. *science* **324**, 1312-1314 (2009).

6 Wang, M. *et al.* Single-crystal, large-area, fold-free monolayer graphene. *Nature* **596**, 519-524 (2021).

7 Gao, L. *et al.* Face-to-face transfer of wafer-scale graphene films. *Nature* **505**, 190-194 (2014).

8 Gao, L. *et al.* Heteroepitaxial growth of wafer scale highly oriented graphene using inductively coupled plasma chemical vapor deposition. *2D Mater.* **3**, 021001 (2016).